

# Effects of large-scale structure on the accuracy of weak lensing mass measurements

Henk Hoekstra<sup>1</sup>, Jan Hartlap<sup>2</sup>, Stefan Hilbert<sup>2,3</sup> & Edo van Uitert<sup>1</sup>

<sup>1</sup>*Leiden Observatory, Leiden University, Niels Bohrweg 2, 2333 CA Leiden, The Netherlands*

<sup>2</sup>*Argelander-Institut für Astronomie, Universität Bonn, Auf dem Hügel 71, 53121 Bonn, Germany*

<sup>3</sup>*Max Planck Institute for Astrophysics, Karl-Schwarzschild-Str. 1, 85741 Garching, Germany*

Accepted. Received; in original form

## ABSTRACT

Weak gravitational lensing has become an important method to determine the masses of galaxy clusters. The intrinsic shapes of the galaxies are a dominant source of uncertainty, but there are other limitations to the precision that can be achieved. In this paper we revisit a typically ignored source of uncertainty: structure along the line-of sight. Using results from the Millennium Simulation we confirm the validity of analytical calculations that have shown that such random projections are particularly important for studies of the cluster density profile. In general the contribution of large-scale structure to the total error budget is comparable to the statistical errors. We find that the precision of the mass measurement can be improved only slightly by modelling the large-scale structure using readily available data.

**Key words:** cosmology: observations – dark matter – large-scale structure of Universe – galaxies: clusters

## 1 INTRODUCTION

The number density of galaxy clusters as a function of mass and redshift can be used to constrain cosmological parameters and probe the growth of structure (e.g., Henry 2000; Borgani et al. 2001; Gladders et al. 2007; Henry et al. 2009; Mantz et al. 2010; Vikhlinin et al. 2009). This approach is conceptually straightforward, but the actual implementation of this method is more difficult. This is because the clusters are identified based on their baryonic properties (e.g., galaxy counts, SZ decrement, X-ray luminosity or temperature), which need to be related to the underlying dark matter distribution. The relation between observed cluster properties and the mass depends itself on the relative importance of the various physical processes that play a role in galaxy and cluster formation. Galaxy clusters provide an excellent laboratory to study these, because multi-wavelength observations provide us with a complete census of the various components: we can actually observe the stars, gas and dark matter content.

The use of clusters to constrain cosmology and to improve our understanding of cluster physics are closely inter-related: feedback processes and differences in formation history lead to variations in the observable properties at a given mass. The resulting intrinsic scatter changes the selection function and thus leads to biased constraints on cosmological parameters if left unaccounted for. Correctly interpreting

the scatter in the scaling relations requires a good understanding of the various sources of uncertainty, which can be either physical or statistical.

A variety of methods can be used to determine the mass of a cluster. Most of these are based on dynamics and assume the cluster is relaxed. In this case, the mass can be obtained from the velocity dispersion of the cluster galaxies. Measurements of the gas pressure, obtained from observations of the hot X-ray emitting intracluster medium (ICM), provide another powerful tracer of the dark matter content. This approach, which assumes hydrostatic equilibrium, has been used extensively, thanks to the high quality observations obtained using powerful X-ray telescopes such as the *Chandra* X-ray Observatory and *XMM-Newton* (e.g., Vikhlinin et al. 2009; Mantz et al. 2010). The interpretation of such measurements is often complicated by the presence of substructures and the fact that most clusters are not relaxed. A major concern is the assumption of hydrostatic equilibrium, because numerical simulations have shown that active galactic nuclei, turbulence, and bulk motions of the gas, as well as variations in the merging history can lead to systematic underestimates of masses based on X-ray observations (e.g., Evrard 1990; Dolag et al. 2005; Rasia et al. 2006; Nagai et al. 2007). Although recent simulations incorporate a wide range of physical processes it is not clear to what extent the simulations provide a realistic estimate of

the systematic error in the mass. It is therefore critical to compare dynamical techniques to methods that do not suffer from these problems.

This is possible thanks to a phenomenon called weak gravitational lensing: the cluster mass distribution perturbs the paths of photons emitted by distant galaxies. As a result the images of these background galaxies appear slightly distorted (or sheared). Unlike dynamical methods, gravitational lensing does not require one to make assumptions regarding the dynamical state of the cluster. The amplitude of this distortion provides us with a direct measurement of the gravitational tidal field, which in turn provides us with an estimate for the projected cluster mass. The recent improvements in sample size and precision allowed Mahdavi et al. (2008) to compare weak lensing and hydrostatic masses for a sample of 18 clusters. Mahdavi et al. (2008) found that at large radii the X-ray results underestimate the mass, in agreement with the findings from numerical simulations. These findings demonstrate the usefulness of weak lensing for multi-wavelength studies of galaxy clusters.

Weak lensing masses are now routinely measured for large samples of clusters (e.g. Hoekstra 2007; Bardeau et al. 2007; Okabe et al. 2010). Tests on simulated data have shown that the best analysis methods can reduce systematic errors in the shear measurements to  $\sim 1 - 2\%$  (Heymans et al. 2006; Massey et al. 2007). Much of the recent progress has been driven by the desire to measure the weak lensing signal caused by intervening large-scale structure, a.k.a. cosmic shear (for a recent review see Hoekstra & Jain 2008). The cosmic shear signal has now been detected at high significance in a number of surveys (e.g., Hoekstra et al. 2002; Van Waerbeke et al. 2005; Hoekstra et al. 2006; Benjamin et al. 2007; Fu et al. 2008; Schrabback et al. 2010) and is one of the most promising tools to study dark energy.

This cosmological signal, however, limits the accuracy with which cluster masses can be determined: the observed lensing signal is a combination of the cluster signal *and* cosmic shear. As first discussed in Hoekstra (2001) the large-scale structure along the line-of-sight is an additional source of noise, but does not bias the measurement of the mass. As shown by Hoekstra (2003) this 'cosmic noise' is particularly relevant when studying cluster mass density profiles (also see Dodelson 2004). Although the effects of uncorrelated structures along the line-of-sight are often acknowledged, their contribution to the formal error budget has typically been ignored. This is somewhat surprising, given that there is little doubt that cosmic shear has been measured.

In this paper we revisit the predictions presented in Hoekstra (2001, 2003) using ray-tracing results from the Millennium Simulation (Springel et al. 2005; Hilbert et al. 2009), demonstrating in §3 once more that cosmic noise should not be ignored in weak lensing studies. We also quantify for the first time the noise introduced by the finite sampling of the source redshift distribution. In §4 we examine whether cosmic noise can be suppressed using readily available data.

## 2 COSMIC NOISE

The observed lensing signal is the combination of the shear induced by the cluster mass distribution *and* that of other structures along the line-of-sight. The expectation value of the latter vanishes, but it does introduce additional variance in the cluster mass estimate. The effect of this cosmic noise on weak lensing cluster studies can be quantified analytically (Hoekstra 2001, 2003) or using numerical simulations (White et al. 2002). Not surprisingly, these studies have shown that the cosmic noise is most important when the cluster signal itself becomes small: i.e., when data at large cluster-centric radii are used, or when clusters at low redshifts are studied. Cosmic noise, however, is also a considerable source of uncertainty for clusters at intermediate redshifts.

Even for a massive cluster, the induced change in the shape of a source galaxy's image is typically small compared to its intrinsic ellipticity. It is therefore convenient to azimuthally average the tangential shear  $\gamma_T$  and study its variation as a function of radius. It can be related to the surface density through

$$\langle \gamma_T \rangle(r) = \frac{\bar{\Sigma}(< r) - \bar{\Sigma}(r)}{\Sigma_{\text{crit}}} = \bar{\kappa}(< r) - \bar{\kappa}(r), \quad (1)$$

where  $\bar{\Sigma}(< r)$  is the mean surface density within an aperture of radius  $r$ , and  $\bar{\Sigma}(r)$  is the mean surface density on a circle of radius  $r$ . The convergence  $\kappa$ , or dimensionless surface density, is the ratio of the surface density and the critical surface density  $\Sigma_{\text{crit}}$ , which is given by

$$\Sigma_{\text{crit}} = \frac{c^2}{4\pi G} \frac{D_s}{D_l D_{ls}}, \quad (2)$$

where  $D_l$  is the angular diameter distance to the lens.  $D_s$  and  $D_{ls}$  are the angular diameter distances from the observer to the source and from the lens to the source, respectively.

The variance in the azimuthally averaged tangential shear in an annulus ranging from  $r_1$  to  $r_2$  caused by large-scale structure along the line-of-sight is given by (Hoekstra 2003):

$$\sigma_{\text{LSS}}^2(r_1, r_2) = 2\pi \int_0^\infty dl l P_\kappa(l) g^2(l, r_1, r_2), \quad (3)$$

where the convergence power spectrum  $P_\kappa(l)$  is given by:

$$P_\kappa(l) = \frac{9H_0^4 \Omega_m^2}{4c^4} \int_0^{w_H} dw \left( \frac{\bar{W}(w)}{a(w)} \right)^2 P_\delta \left( \frac{l}{f_K(w)}; w \right). \quad (4)$$

Here  $w$  is the radial coordinate,  $a(w)$  the cosmic scale factor, and  $f_K(w)$  the comoving angular diameter distance.  $P_\delta(l; w)$  is the matter power spectrum. We consider relatively small scales, and therefore need to account for the non-linear evolution (e.g. Jain & Seljak 1997; Schneider et al. 1998; Hilbert et al. 2009).  $\bar{W}(w)$  is the average ratio of angular diameter distances  $D_{ls}/D_s$  for a redshift distribution of sources  $p_w(w)$ :

$$\bar{W}(w) = \int_w^{w_H} dw' p_w(w') \frac{f_K(w' - w)}{f_K(w')}. \quad (5)$$

The function  $g(l, r_1, r_2)$  in Eqn. (3) is a filter of the convergence power spectrum and is specified by our choice to consider the azimuthally averaged tangential shear. We refer to Hoekstra (2003) for a more detailed discussion, including the expression for  $g(l, r_1, r_2)$ . In this paper we measure the azimuthally averaged tangential shear as a function of radius  $r = (r_1 + r_2)/2$ , in bins that are  $r_2 - r_1 = 15$  arcseconds wide.

## 2.1 Source redshift sampling

In this paper we identify another source of error, which is important for high redshift clusters and at small radii. It arises because the amplitude of the lensing signal depends on the redshift of the sources. At large distances from the cluster, the signal is obtained by averaging over a relatively large number of galaxies, thus sampling the average redshift distribution fairly well. However, at small radii the number of sources is much smaller leading to a large variance in the actual redshift distribution  $n(z)$ . This problem can be dealt with using photometric redshifts for the sources, but the required increase in observing time may make this difficult to achieve in practice. This sampling variance depends on the width of the redshift distribution and can be estimated from observations of blank fields (e.g., Ilbert et al. 2006, 2009). This estimate, however, does not account for the clustering of the source galaxies, which increases the scatter further. To include the effects of source clustering one can place corresponding apertures in observed fields with redshifts and measure the scatter. This approach, however, does require a rather large survey area. To quantify how the *combination* of distant (i.e., uncorrelated) large-scale structure and variations in the source redshift distribution affect weak lensing mass determinations we need a realistic distribution of source galaxies, which themselves are part of the large-scale structure. This requires mock data sets based on cosmological numerical simulations of a large area.

## 2.2 Numerical simulations

We use results from the Millennium Simulation (Springel et al. 2005), which is a large  $N$ -body simulation following the evolution of  $2160^3$  dark matter particles in a periodic box with a side length of  $500 h^{-1}$  Mpc, using a flat  $\Lambda$ CDM cosmology<sup>1</sup>. The lensing signal is obtained from a careful ray-tracing analysis presented in detail in Hilbert et al. (2009). The simulation is carried out by dividing the periodically continued matter distribution of the Millennium Simulation into 36 slices out to  $z = 3$ , each with a thickness of  $\approx 100 h^{-1}$  Mpc. These are subsequently projected onto lens planes, and a set of light rays is propagated through the array of planes. Using a set of recursion relations, the ray positions on each plane and the Jacobian matrices for the light paths from the observer to each plane are obtained. Different realizations are obtained by choosing different observer positions, in our case yielding

<sup>1</sup> The values for the cosmological parameters that were adopted are: a matter density of  $\Omega_m = 0.25$ , a cosmological constant with  $\Omega_\Lambda = 0.75$ , a Hubble constant of  $H_0 = 73 \text{ km/s/Mpc}$ , a spectral index  $n = 1$  and a normalisation  $\sigma_8 = 0.9$  for the primordial power spectrum of density fluctuations.

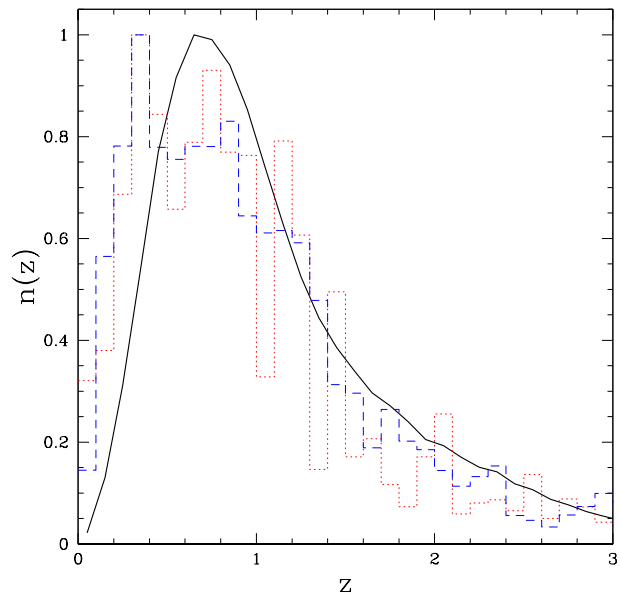


**Figure 1.** Redshift distribution  $n(z)$  of the simulated source galaxies, with apparent magnitudes  $r < 25$  (solid line). For comparison redshift histograms for the COSMOS survey (red dotted histogram; Ilbert et al., 2009) and the CFHTLS (blue dashed histogram; Ilbert et al., 2005) are shown (same selection in apparent magnitude). The difference may be due to limitations of the simulation, but may also reflect incompleteness at high redshifts in the case of the photometric redshift catalogs. Nonetheless, the redshift distribution derived from the simulations is adequate for our study.

512 patches of one square degree each. The periodic repetition of structures along the line-of-sight, which is caused by the finite volume of the Millennium Simulation, is minimized by choosing a line-of-sight direction that encloses carefully chosen angles with the faces of the simulation box. The advantage of this approach is that the matter distribution remains continuous across slice boundaries, so that correlations on scales larger than the thickness of the redshift slices are maintained.

Information on the properties of galaxies is obtained from the semi-analytic models of galaxy formation by De Lucia & Blaizot (2007). Combined with the ray-tracing results, this allows us to obtain realistic lensed positions and magnitudes for each galaxy, together with shear and convergence at the galaxies' locations. For our galaxy catalogues, we impose a magnitude cut of  $r_{\text{SDSS}} < 25$ . The average redshift distribution of these source galaxies is presented in Figure 1. The results agree fairly well with photometric redshift distributions from the COSMOS survey (Ilbert et al. (2009); red dotted histogram) and the CFHT Legacy Survey (Ilbert et al. (2006); blue dashed histogram). The actual redshift distributions appear to peak at somewhat lower redshift, but this difference is not important for the study presented here.

### 2.3 Cluster Signal

The numerical simulations provide a realistic lensing signal that would be observed in a random patch of sky. This signal is also present when a cluster of galaxies is studied: the observed lensing signal is the combination of that of the cluster and the distant large-scale structure (distant in the sense that it does not know about the cluster). To simulate this, we can simply add the cluster signal to that from the simulations. We assume that the density profile of a cluster is described by the NFW (Navarro et al. 1997) profile

$$\rho(r) = \frac{M_{\text{vir}}}{4\pi f(c)} \frac{1}{r(r+r_s)^2}, \quad (6)$$

where  $M_{\text{vir}}$  is the virial mass, the mass enclosed within the radius  $r_{\text{vir}}$ . The virial radius is related to the scale radius  $r_s$  through the concentration  $c = r_{\text{vir}}/r_s$  and the function  $f(c) = \ln(1+c) - c/(1+c)$ . By definition, the virial mass and radius are related through

$$M_{\text{vir}} = \frac{4\pi}{3} \Delta_{\text{vir}}(z) \rho_{\text{bg}}(z) r_{\text{vir}}^3, \quad (7)$$

where  $\rho_{\text{bg}} = 3H_0^2 \Omega_m (1+z)^3 / (8\pi G)$  is the mean density at the cluster redshift and the virial overdensity  $\Delta_{\text{vir}} \approx (18\pi^2 + 82\xi - 39\xi^2) / \Omega_m(z)$ , with  $\xi = \Omega_m(z) - 1$  (Bryan & Norman 1998). For the  $\Lambda$ CDM cosmology considered here,  $\Delta_{\text{vir}}(0) = 337$ . Expressions for the surface density and tangential shear of the NFW profile have been derived by Bartelmann (1996) and Wright & Brainerd (2000) and we refer the interested reader to these papers for the relevant equations.

In simulations of collisionless cold dark matter the NFW density profile provides a good description of the radial mass distribution for halos with a wide range in mass (e.g., Navarro et al. 1995, 1997). The density profile is described by specifying  $M_{\text{vir}}$  and concentration  $c$  (or equivalently  $r_s$ ). Numerical simulations, however, indicate that the average concentration depends on the halo mass and the redshift (Navarro et al. 1995; Bullock et al. 2001; Duffy et al. 2008). To account for this correlation we use the relation between the virial mass  $M_{\text{vir}}$  and concentration  $c$  from Duffy et al. (2008) who studied numerical simulations using the best fit parameters of the WMAP5 cosmology<sup>2</sup> (Komatsu et al. 2009). The best fit  $c(M_{\text{vir}})$  is given by:

$$c = 7.85 \left( \frac{M_{\text{vir}}}{2 \times 10^{12}} \right)^{-0.081} (1+z)^{-0.71}. \quad (8)$$

Simulations show considerable variation in the density profiles, resulting in a lognormal distribution of  $c$  with a scatter  $\sigma_{\log c} \sim 0.1$  for halos of a given mass (e.g., Jing 2000; Neto et al. 2007). Furthermore, Neto et al. (2007) showed that the concentration distributions are different for 'relaxed' and 'unrelaxed' halos. Although these physical variations are an additional source of uncertainty when attempting to constrain the mass-concentration relation observationally, they are not relevant for our study of cosmic noise.

<sup>2</sup> This is a different cosmology from the one used to run the Millennium Simulation, but we note that the actual choice of mass-concentration relation is not important for the main results presented in this paper.

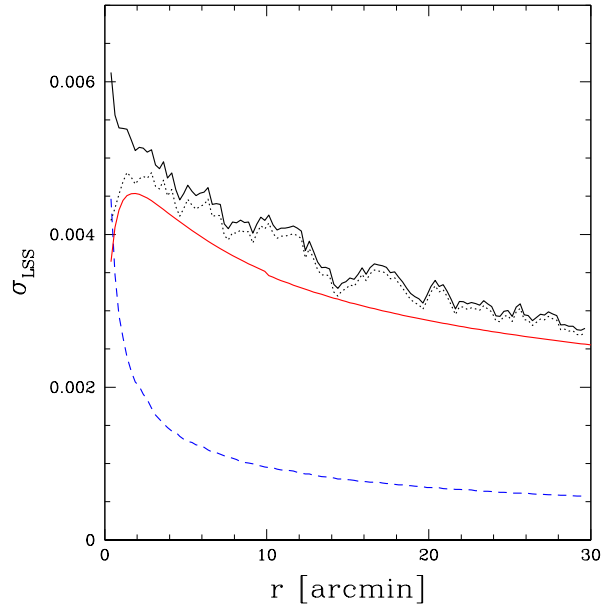


**Figure 2.** The dispersion  $\sigma_{\text{LSS}} = \langle \gamma_T^2 \rangle^{1/2}$  introduced by distant large scale structure. The solid black line shows the dispersion measured from the 512 realisations from the Millennium Simulation. At small radii the small number of sources introduces additional scatter (indicated by the dashed blue curve). The smooth red line corresponds to the analytical prediction from Hoekstra (2003). The prediction does not account for noise arising from the finite number of sources and should be compared to the dotted black line (which is corrected for this effect). The prediction is about 15% lower, which is due to the adopted non-linear power spectrum (see text and Hilbert et al. 2009).

### 3 RESULTS

For each of the 512 realisations from the Millennium Simulation we measure the azimuthally averaged tangential shear as a function of radius from the centre of the image. The solid black line in Figure 2 shows the resulting dispersion  $\sigma_{\text{LSS}} = \langle \gamma_T^2 \rangle^{1/2}$  as determined from the 512 realisations. The prediction based on the Peacock & Dodds (1996) prescription for the non-linear evolution of the power spectrum is indicated by the red line. On large scales ( $> 5'$ ) the prediction is about 15% lower, which we attribute to the adopted non-linear power spectrum. This difference is consistent with the conclusions of Hilbert et al. (2009) who compared various prescriptions for the non-linear power spectrum.

Close pairs of galaxies are sheared by similar amounts if all sources are at the same redshift. In this case, the dispersion in the tangential shear in a given radial bin would be small (for a given realisation). This is not true for actual observations, because the source redshift distribution is broad (see Figure 1). At large radii, where the signal is averaged over many galaxies, the source redshift distribution is expected to be close to the average. At small radii this is not a good representation, because the small number of sources samples the average distribution only sparsely. This leads to additional noise if photometric redshifts for the sources are not available. Unlike the distant large-scale structure, this effect is only relevant at small radii.

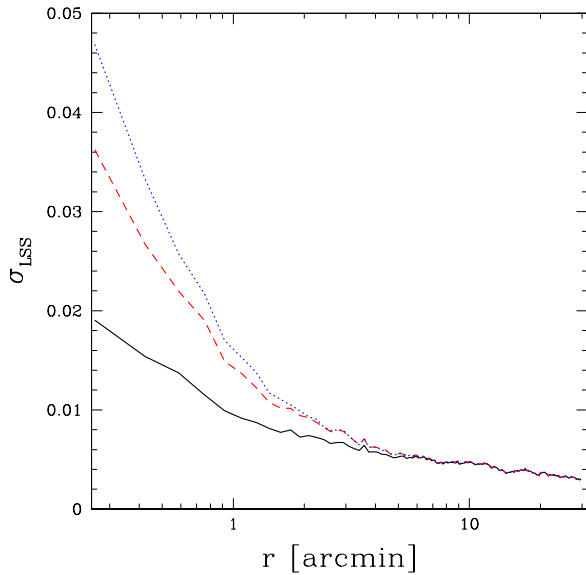


**Figure 3.** The dispersion  $(\gamma_T^2)^{\frac{1}{2}}$  for a cluster with  $M_{\text{vir}} = 10^{15} M_{\odot}$  with redshift  $z = 0.2, 0.4$  and  $0.6$  (solid-black, dashed-red and dotted blue lines, respectively). At large radii the cosmic shear contribution, which is independent of cluster redshift dominates the dispersion. On small scales, the dispersion in source redshifts increases with lens redshift.

On small scales we can assume that the dispersion in the tangential shear for a single realisation is predominantly caused by the spread in source redshifts. The resulting mean dispersion as a function of radius is indicated by the dashed blue curve in Figure 2. This is the contribution to  $\sigma_{\text{LSS}}$  caused by the finite sampling of the source redshift distribution. If we remove this source of scatter, the agreement between the Hoekstra (2003) prediction and the Millennium Simulation is excellent (as indicated by the dotted line), keeping in mind the difference in amplitude of the non-linear power spectrum based on Peacock & Dodds (1996). Hence, variations in the actual source redshift distribution lead to an increase in the observed variance at radii  $\lesssim 4'$ . Most of the noise caused by the lack of photometric redshifts arises from the fact the redshift distribution is broad, but we expect that the scatter is boosted by the fact that sources are in fact clustered. Comparison with the simulations confirms this, but the increase in scatter is modest: the increase is only  $\sim 20\%$  compared to the estimate based on the  $n(z)$  alone.

The lack of knowledge of the actual source redshift distribution contributes to the uncertainty in the cluster mass because it leads to scatter in the ratio  $\beta = D_{ls}/D_s$  in the expression for the critical surface density. For a low redshift cluster most sources are at much higher redshifts and  $\beta \sim 1$ . Consequently the variation in  $\beta$  is small. As the redshift of the lens is closer to the mean source redshift, the variation in  $D_{ls}/D_s$  increases. This is demonstrated in Figure 3, which shows the dispersion for a cluster with mass  $M_{\text{vir}} = 10^{15} M_{\odot}$  at various redshifts. At large radii the variation in the redshift distribution is negligible and the dispersion converges

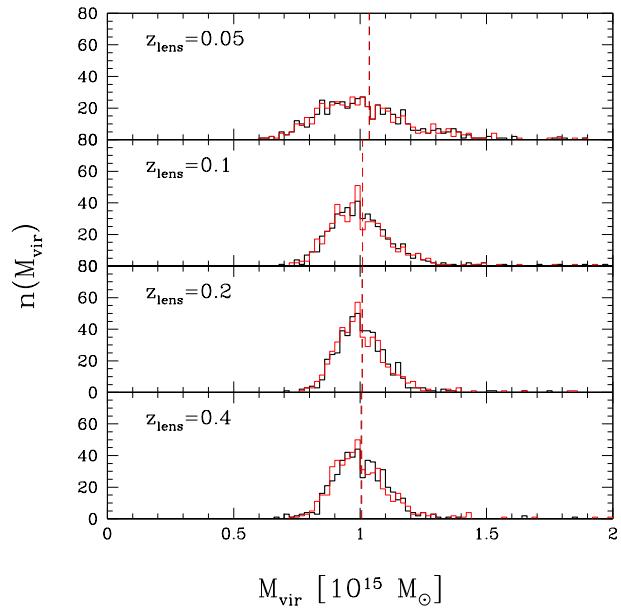


**Figure 4.** Histogram of the best fit virial masses  $M_{\text{vir}}$  for the 512 realisations for lenses at  $z = 0.05, 0.1, 0.2$  and  $0.4$ , when we adopt the mass-concentration relation from Duffy et al. (2008). The red histograms show the distribution of results when only distant large scale structure is considered. For low redshifts the distribution of masses is skewed, but the average remains unbiased (indicated by the vertical dashed line). The black histograms show the results when the variation in the source redshift distribution is included. Note that these results do not include any shape noise.

to the cosmic shear signal. At small radii, the scatter caused by the variation in the source redshift distribution increases rapidly with cluster redshift. Note that deeper observations will improve the sampling of the redshift distribution because of the larger number of sources. However, at the same time the average source redshift will increase, resulting in a larger cosmic noise contribution (see Hoekstra 2001).

### 3.1 Mass estimates

In this section we study the combined effect of cosmic noise and the finite sampling of the source redshift distribution on the weak lensing mass estimate of a cluster with a virial mass  $M_{\text{vir}} = 10^{15} M_{\odot}$ . We assume it follows an NFW profile with the concentration given by Eqn. (8) and add the corresponding lensing signal to the shear inferred from the ray-tracing analysis, yielding 512 realisations of the cluster lensing signal. We fit an NFW model to the resulting lensing signal out to an outer radius  $R_{\text{out}}$ . The innermost point is  $7''.5$ , but the results do not depend much on this choice: the small number of sources at these radii means they have a low statistical weight in the fit. We consider only shape noise as a source of uncertainty and determine the best fit masses from a standard least-squares fit.

We first consider the case where  $M_{\text{vir}}$  is the only parameter that is fit, because the concentration is specified through Eqn. 8. Figure 4 shows the resulting distribution of masses for clusters at various redshifts if we fit the NFW

**Table 1.** Dispersion in  $M_{\text{vir}}$  and  $c$ 

$z_{\text{lens}}$	adopting $c(M)$		$M_{\text{vir}}$ & $c$ free parameters			
	$R_{\text{out}}=10'$	$R_{\text{out}}=25'$	$R_{\text{out}}=10'$	$R_{\text{out}}=25'$	$R_{\text{out}}=10'$	$R_{\text{out}}=25'$
	$\sigma_M$	$\sigma_M$	$\sigma_M$	$\sigma_c$	$\sigma_M$	$\sigma_c$
LSS only						
0.05	0.25	0.22	0.69	0.82	0.43	0.81
0.1	0.15	0.17	0.35	0.53	0.25	0.63
0.2	0.12	0.15	0.21	0.44	0.21	0.59
0.4	0.13	0.18	0.21	0.48	0.23	0.69
0.6	0.18	0.24	0.28	0.61	0.29	0.88
variation in $n(z)$ only						
0.05	0.01	0.01	0.01	0.04	0.01	0.03
0.1	0.02	0.01	0.02	0.08	0.01	0.06
0.2	0.03	0.02	0.03	0.25	0.02	0.23
0.4	0.07	0.06	0.05	0.33	0.05	0.31
0.6	0.10	0.08	0.08	0.45	0.07	0.41
combination of LSS and variation in $n(z)$						
0.05	0.25	0.22	0.73	0.83	0.44	0.81
0.1	0.14	0.16	0.40	0.56	0.24	0.65
0.2	0.11	0.14	0.23	0.54	0.21	0.67
0.4	0.12	0.15	0.22	0.65	0.21	0.82
0.6	0.16	0.22	0.28	0.85	0.26	1.08
statistical						
0.05	0.17	0.10	0.93	1.27	0.16	0.66
0.1	0.12	0.08	0.25	0.81	0.10	0.54
0.2	0.10	0.07	0.15	0.65	0.09	0.52
0.4	0.12	0.10	0.15	0.73	0.11	0.63
0.6	0.17	0.14	0.19	1.00	0.15	0.89

Dispersions in the values for the best-fit virial mass  $M_{\text{vir}}$  (in units of  $10^{15}M_{\odot}$ ) and concentration  $c$  as a function of lens redshift and the maximum radius that is used in the fit. We list results for the effects of distant large-scale structure and variation in the source redshift distribution separately and combined. These results do not include the statistical error due to the intrinsic ellipticities of the source galaxies. The statistical errors (but now without LSS contributions) are given in the fourth set of results.

model out to  $R_{\text{out}} = 10'$ . For low redshifts the distribution is somewhat skewed, but the mean value is unbiased (as indicated by the vertical dashed lines). Table 1 lists the values for the scatter  $\sigma_M$  caused by the combined effects of cosmic noise and source redshift variation. Comparison with the statistical errors (computed assuming a total intrinsic source ellipticity of 0.3) shows that the cosmic noise contribution is quite comparable at all redshifts. Cosmic noise is minimal at intermediate redshifts ( $0.2 < z < 0.4$ ).

The increase for  $z > 0.4$  is caused by the fact that the angular extent of the cluster decreases, whereas the aperture  $R_{\text{out}}$  is kept fixed. The dashed lines in Figure 5 show how the cosmic noise depends on  $R_{\text{out}}$ . For reference, Table 1 also lists the values for  $\sigma_M$  for  $R_{\text{out}} = 25'$ . For  $z = 0.05$  (black line) the cosmic noise decreases with aperture size, but at higher redshifts it increases. However, the statistical uncertainty decreases with increasing  $R_{\text{out}}$ , as indicated by the dotted lines. The solid lines indicate the net result: for  $z = 0.05$  there is a net gain, but for a cluster with  $z > 0.2$  (blue line) there is no benefit extending the fit beyond  $10'$ .

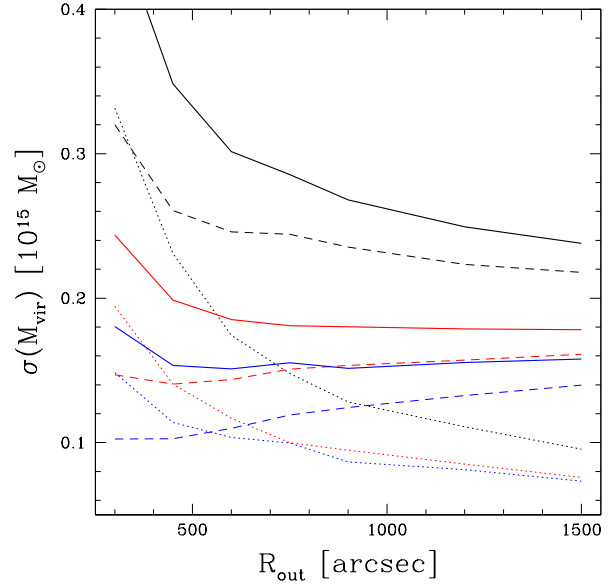


**Figure 5.** The solid lines show the total uncertainty in the best-fit virial mass (for  $M_{\text{vir}} = 10^{15}M_{\odot}$ ) as a function of the maximum radius used to fit the NFW for a lens redshift of  $z = 0.05$  (black),  $z = 0.1$  (red) and  $z = 0.2$  (blue). The contribution from the shape noise (i.e., statistical error) is indicated by the dotted curves, whereas the dashed lines show the LSS contribution. For  $z = 0.05$  there is a clear benefit from wide-field imaging data, but at  $z = 0.2$  the uncertainty is flat for  $R_{\text{out}} > 10'$ .

We also compare the relative contributions of the distant large-scale structure and the variation in  $n(z)$ . The latter is computed by using the simulated redshift distribution, but without adding the cosmic noise to the cluster signal. To compute the former, we add the cluster shear computed for the average source redshift to the ray-tracing results. Interestingly, the combined effect of LSS and variation in  $n(z)$  is to slightly reduce the scatter in the recovered masses, compared to the LSS-only case. This can be easily understood: a structure at lower redshift will increase the lensing signal, but will also increase the number of sources at these redshifts. As the latter are lensed less than the average source, they partly offset the increase in lensing signal. Note that the combined effect does not bias the cluster mass estimates.

The lensing signal of high redshift clusters can be boosted by removing foreground galaxies using photometric redshift information and optimally weighing the remaining sources based on their  $D_{ls}/D_s$ . However, the cosmic noise increases also rapidly with source redshift:  $\sigma_{\text{LSS}} \propto z^{1.4}$  for ( $z < 1$ ), which might limit the expected improvement in precision. The redshift distribution used here drops quickly beyond  $z \sim 1$  and we find that for clusters with  $z > 0.4$  the photometric redshift information does improve the mass measurements.

### 3.2 Joint constraints on mass and concentration

So far we examined the effect of cosmic noise when one assumes a mass-concentration relation which is based on nu-



merical simulations. Instead, many studies fit the lensing signal with both  $M_{\text{vir}}$  and  $c$  as free parameters. This allows one to directly constrain the concentration and therefore test the numerical simulations (e.g., Clowe & Schneider 2002; Hoekstra et al. 2002; Mandelbaum et al. 2008; Okabe et al. 2010). Cosmic noise, however, significantly increases the formal uncertainties in such measurements (Hoekstra 2003). Figure 6 shows the distribution of best fit values for  $M_{\text{vir}}$  and concentration  $c$  for the 512 realisations when fitting both parameters simultaneously. The contours indicate the statistical uncertainties in the parameters, whereas the points show the spread due to cosmic noise and variation in the source redshift distribution. Table 1 lists the scatter in the parameters. It is clear that cosmic noise has a large impact on the ability to constrain the concentrations. In particular, note the outliers with high inferred masses and low concentrations.

We also examined whether cosmic noise biases the slope of the mass-concentration relation that is inferred from studies of samples of clusters. For instance, Okabe et al. (2010) obtain a power-law slope of  $0.40 \pm 0.19$ , which is steeper than is seen in numerical simulations. They examined the correlation in parameters due to the shape noise for simulated profiles with masses  $M_{\text{vir}} = 0.2 - 1.5 \times 10^{15} M_{\odot}$ . Okabe et al. (2010) find a bias of 0.06, much smaller than the observed value. We performed a similar test and find that cosmic noise also biases the inferred slope, but by a similar amount. The combined effect of shape and cosmic noise is a bias of only 0.08 in the slope, because the correlation between  $M_{\text{vir}}$  and  $c$  is similar for both sources of error. We note that the inferred slope is steeper if smaller range in mass is considered: we find a bias of 0.17 for a range  $M_{\text{vir}} = 1 - 1.5 \times 10^{15} M_{\odot}$ . Hence, the most important consequence of including cosmic noise is to reduce the significance of the measurement of the slope of the mass-concentration relation.

## 4 REDUCING COSMIC NOISE

The results presented in the previous section indicate that weak lensing studies should include cosmic noise in their error budget. An interesting question is whether one can reduce, or even remove, the effects of cosmic noise. A statistical approach was discussed by Dodelson (2004) who proposed a minimum variance estimator to account for cosmic noise in mass reconstructions. A concern, however, is that substructures associated with the cluster might be suppressed as well.

### 4.1 Accounting for additional clusters

In this section we will explore whether the observations themselves can be used to reduce the cosmic noise. Although one can imagine many different ways to predict the cosmic noise signal, we will consider a relatively simple method. It requires only a minimum of colour information and is therefore readily available: most studies include (some) color information to identify cluster members.

Massive collapsed structures, such as galaxy clusters and groups of galaxies contribute a large fraction of the power on the physical scales relevant for cosmic noise. Fortunately they can be identified in multi-colour data, similar

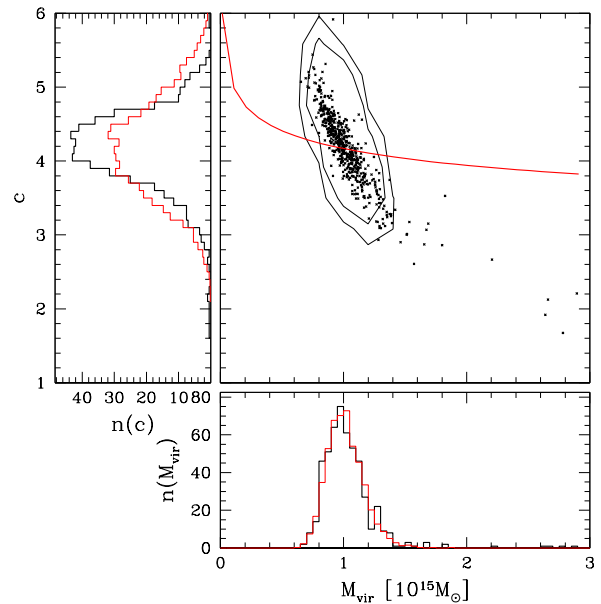


**Figure 6.** Distribution of best-fit  $M_{\text{vir}}$  and  $c$  when both parameters are free to vary. The points indicate the spread in results when distant large-scale structure and source redshift variation are included. The contours indicate the regions that enclose 68% and 90% of the fits when only statistical (shape) noise is considered. The red line shows the mass-concentration relation from Duffy et al. (2008).

to what is done in optical cluster surveys. The most massive systems can readily be located using a red-sequence method (e.g., Gladders & Yee 2000). Photometric redshifts, involving more colours, can be used to find lower mass halos. For instance, Milkeraitis et al. (2010) used the Millennium Simulation to examine how well one can identify clusters using five optical filters. They find that clusters with masses larger than  $\sim 5 \times 10^{13}$  can be detected with fairly high completeness ( $\sim 80\%$ ) and low false detection rate ( $\sim 20\%$ ).

After having identified the clusters one needs to estimate their contribution to the lensing signal. Here we take an optimistic approach and assume we can find all halos down to a virial mass limit  $M_{\text{lim}}$ . In practice such a clear mass limit may be more difficult to achieve. We fit these halos simultaneously with the cluster of interest (where we ignore shape noise and assume the halos follow an NFW profile with our adopted mass-concentration relation). For a limiting mass  $M_{\text{lim}} = 5 \times 10^{13} M_{\odot}$  on average 5.4 halos are fit in addition to the input cluster (with actual numbers ranging from 0 to 12). We find that this procedure does not bias the recovered cluster mass.

Figure 7 shows the resulting scatter in the best fit virial mass as a function of the mass limit of the halos included in the fit. The solid lines show the results when the NFW model is fit out to  $10'$ , whereas the dashed lines show the results for  $R_{\text{out}} = 25'$ . For reference, the left panel indicates the corresponding statistical uncertainties in the virial mass due to the shape noise.

The results suggest our simple approach is indeed able to reduce the effect of cosmic noise. Figure 7 shows that this

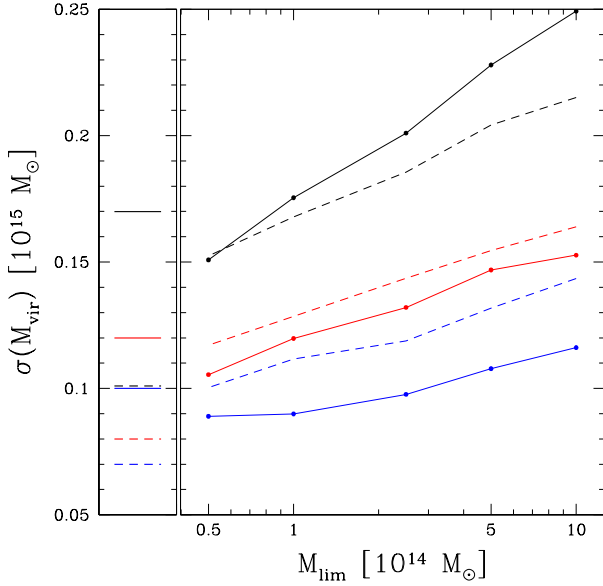


**Figure 7.** The scatter in the best-fit virial mass (for  $M_{\text{vir}} = 10^{15} M_{\odot}$ ) as a function of  $M_{\text{lim}}$ , the minimum mass of halos that are fit simultaneously with the cluster of interest. The improvement is largest for a cluster at  $z = 0.05$  (black line). The benefits are smaller for  $z = 0.1$  (red line) and  $z = 0.2$  (blue line). The solid lines show the results when the NFW model is fit out to  $10'$ , whereas the dashed lines show the results for  $R_{\text{out}} = 25'$ . For reference, the left panel shows the statistical uncertainty in the virial mass due to the intrinsic shapes of the source galaxies.

is most relevant for clusters at very low redshifts. However, even with a (low) mass limit of  $M_{\text{lim}} = 5 \times 10^{13} M_{\odot}$ , the cosmic noise remains a dominant source of uncertainty. We have examined several other approaches, such as using the luminosities of galaxies to predict the lensing signal, and found that none is able to significantly improve upon the relatively simple approach outlined above. We now will attempt to understand why this is.

## 4.2 Limitations

To compute the cosmic noise signal in §3 we need the non-linear power spectrum of density fluctuations to account for the fact that collapsed halos increase the power on small scales. In general it is computed using (fitting functions to) numerical simulations, such as the prescription of Peacock & Dodds (1996) that we used here. The observation that dark matter halos are well described by NFW profiles allows for an analytic approach as suggested by Seljak (2000). In this model the abundance of halos is given by the halo mass function and their clustering is described by a mass dependent bias relation. The dark matter profiles themselves are described by spherical NFW profiles that are functions of the mass only (i.e., they follow a mass-concentration relation). The resulting power spectrum is the sum of the contribution from a Poisson term that corresponds to individual halos  $P^{\text{P}}(k)$  and a term arising from the clustering of halos  $P^{\text{hh}}(k)$  themselves. This halo-model

has proven to be useful to study the clustering of galaxies and interpret the galaxy-mass cross-correlation function. On small scales the Poisson term dominates. It is given by

$$P^{\text{P}}(k) = \frac{1}{(2\pi)^3} \int d\nu f(\nu) \frac{M(\nu)}{\bar{\rho}} |y(k, M(\nu))|^2, \quad (9)$$

where  $\bar{\rho}$  is the mean matter density and  $y(k, M)$  is the ratio of the Fourier transform of the halo profile  $\hat{\rho}(k)$  and the halo mass  $M(\nu)$ . The peak height  $\nu$  of such an overdensity is given by

$$\nu = \left[ \frac{\delta_c(z)}{\sigma(M)} \right]^2, \quad (10)$$

where  $\delta_c$  is the value of a spherical overdensity at which it collapses at a redshift  $z$ .  $\sigma(M)$  is the rms fluctuation in spheres that contain mass  $M$  at an initial time, extrapolated to  $z$  using linear theory. The function  $f(\nu)$  is related to the halo mass function  $dn/dM$  through

$$\frac{dn}{dM} dM = \frac{\bar{\rho}}{M} f(\nu) d\nu. \quad (11)$$

We use the expressions from Sheth et al. (2001) for  $f(\nu)$  and the  $M(c)$  relation from Duffy et al. (2008) to compute the Poisson term. The halo-halo term is important on large scales and is computed by integrating over the mass function with the halo bias  $b(\nu)$  and Fourier transform of the density profile

$$P^{\text{hh}}(k) = P_{\text{lin}}(k) \left( \int d\nu f(\nu) b(\nu) y(k, M(\nu)) \right)^2, \quad (12)$$

where  $P_{\text{lin}}(k)$  is the linear power spectrum.

The black line in Figure 8 shows the cosmic noise (LSS-only) measured from the simulations. The dashed black line is the halo model prediction, where the Poisson term has been multiplied by 1.15 to match the simulations. The solid red line in Figure 8 shows  $\sigma_{\text{LSS}}$  if we fit all halos with  $M_{\text{vir}} > 5 \times 10^{13} M_{\odot}$  as described in the previous section. The theoretical limit of the reduction in power by accounting for massive halos along the line-of-sight is obtained by integrating Eqns. (9) and (12) up to  $M_{\text{lim}}$ , rather than extending the integral over all masses. The dashed line in Figure 8 shows the corresponding result for  $M_{\text{lim}} = 5 \times 10^{13} M_{\odot}$ . It is clear that this estimate overestimates the reduction in cosmic noise, compared to the actual simulated results.

The reason for this is simple: the theoretical limit implicitly assumes that the halo masses were determined perfectly, which clearly is too optimistic. Differences in the true mass  $M_t$  and the fitted mass  $M_f$  add additional power to the theoretical limit. For the Poisson term the residual power  $P^{\text{P res}}$  is given by:

$$P^{\text{P res}}(k) = \frac{1}{(2\pi)^3} \int_{M_{\text{lim}}}^{\infty} d\nu f(\nu) \frac{M_t(\nu)}{\bar{\rho}} \times \int_0^{\infty} dM_f |y(k, M_t) - y(k, M_f)|^2 W(M_t - M_f), \quad (13)$$



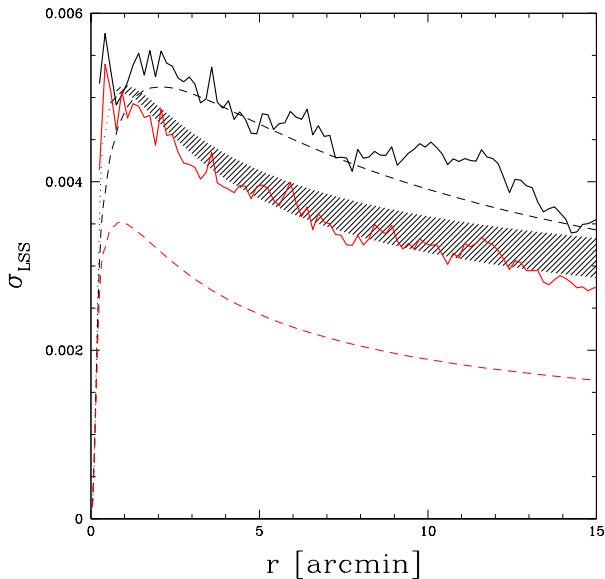


**Figure 8.** The cosmic noise signal (LSS-only) as a function of radius. The black line is the total signal and the dashed black line is the signal from the halo model. The Poisson term in the halo model has been multiplied by 1.15 to match the simulations. The solid red line indicates the cosmic noise when halos with  $M_{\text{vir}} > 5 \times 10^{13} M_{\odot}$  are included in the fit (see text for details). The red dashed line shows the halo model signal if such halos are removed perfectly. The dashed region indicates our estimate for the range in scatter when the uncertainties are taken into account.

where  $W(M_t - M_f)$  describes the distribution of the difference between the true and recovered masses. Comparison with the simulations shows that  $W$  can be approximated by a Gaussian with a dispersion  $\sigma$  that depends on the halo mass, with  $\sigma = 2.3 \times 10^{13} M_{\odot} + 0.28 \times M_t$ . We need to add the contribution  $P^{\text{hh}}$  to  $P_{\text{res}}^{\text{P}}$ , which in the ideal case is integrated up to  $M_{\text{lim}}$ . However, we cannot fit the contributions from halos outside the field of view and the actual halo-halo contribution will lie between the ideal case and the full  $P^{\text{hh}}$ .

The shaded region in Figure 8 indicates the expected range in  $\sigma_{\text{LSS}}$  when we account for the uncertainties in the modelling. The actual results agree very well with our estimates based on the halo model. In reality the situation is even more dire, because we ignored shape noise in the calculations presented here.

## 5 CONCLUSIONS

We used the Millennium Simulation to study how large-scale structure along the line-of-sight (cosmic noise) affects the uncertainty in the weak lensing masses of clusters of galaxies. After accounting for differences in the calculation of the non-linear power spectrum of density fluctuations, analytical estimates agree well with the simulations. The simulations therefore support the findings by Hoekstra (2001, 2003) that cosmic noise is a relevant source of uncertainty in weak lensing mass determinations and therefore should be included in

the reported error budget. We do note that the adopted  $\sigma_8$  in the simulation is higher than the currently favoured value, which reduces the amplitude of the cosmic noise somewhat.

We also examined whether variations in the source galaxy redshift distribution are an important source of uncertainty. Although the importance increases with the redshift of the cluster, we find it is never significant when compared to statistical errors or cosmic noise. For the simulated redshift distribution of sources used here we find that source redshift information improves the precision of the mass measurement, because the boost in lensing signal by the removal of foreground galaxies is larger than the increase in cosmic noise due to the increase in the mean source redshift.

Finally we examined whether it is possible to reduce the effect of cosmic noise by identifying galaxy clusters and groups along the line-of-sight. Such structures can be located fairly easily in multi-colour data. We study a simple approach where we fit the masses of these additional structures down to a mass  $M_{\text{lim}}$  and find that cosmic noise can indeed be reduced, in particular for clusters at very low redshifts ( $z \sim 0.05$ ). Nonetheless, the cosmic noise remains a dominant source of uncertainty. To better understand the limitations of modelling the contribution from distant large-scale structure, we computed the expected signals using the halo model. We find that the uncertainties (or variations) in the profiles fundamentally limit the suppression of cosmic noise. As a consequence, cosmic noise will remain a dominant source of uncertainty in weak lensing cluster mass measurements, and should not be ignored.

## ACKNOWLEDGMENTS

The authors would like to thank Tim Schrabback for useful comments. JH and SH acknowledge support by the Deutsche Forschungsgemeinschaft within the Priority Programme 1177 under the project SCHN 342/6 and by the German Federal Ministry of Education and Research (BMBF) through the TR33 ‘‘The Dark Universe’’. HH acknowledges support from the Netherlands Organization for Scientific Research (NWO) and a Marie Curie International Reintegration Grant.

## REFERENCES

- Bardeau S., Soucail G., Kneib J., Czoske O., Ebeling H., Hudelot P., Smail I., Smith G. P., 2007, *A&A*, 470, 449
- Bartelmann M., 1996, *A&A*, 313, 697
- Benjamin J., Heymans C., Semboloni E., van Waerbeke L., Hoekstra H., Erben T., Gladders M. D., Hettterscheidt M., Mellier Y., Yee H. K. C., 2007, *MNRAS*, 381, 702
- Borgani S., Rosati P., Tozzi P., Stanford S. A., Eisenhardt P. R., Lidman C., Holden B., Della Ceca R., Norman C., Squires G., 2001, *ApJ*, 561, 13
- Bryan G. L., Norman M. L., 1998, *ApJ*, 495, 80
- Bullock J. S., Kolatt T. S., Sigad Y., Somerville R. S., Kravtsov A. V., Klypin A. A., Primack J. R., Dekel A., 2001, *MNRAS*, 321, 559
- Clowe D., Schneider P., 2002, *A&A*, 395, 385
- De Lucia G., Blaizot J., 2007, *MNRAS*, 375, 2
- Dodelson S., 2004, *Phys. Rev. D*, 70, 023008

- Dolag K., Vazza F., Brunetti G., Tormen G., 2005, *MNRAS*, 364, 753
- Duffy A. R., Schaye J., Kay S. T., Dalla Vecchia C., 2008, *MNRAS*, 390, L64
- Evrard A. E., 1990, *ApJ*, 363, 349
- Fu L., Semboloni E., Hoekstra H., Kilbinger M., van Waerbeke L., Tereno I., Mellier Y., Heymans C., Coupon J., Benabed K., Benjamin J., Bertin E., Doré O., Hudson M. J., Ilbert O., Maoli R., Marmo C., McCracken H. J., Ménard B., 2008, *A&A*, 479, 9
- Gladders M. D., Yee H. K. C., 2000, *AJ*, 120, 2148
- Gladders M. D., Yee H. K. C., Majumdar S., Barrientos L. F., Hoekstra H., Hall P. B., Infante L., 2007, *ApJ*, 655, 128
- Henry J. P., 2000, *ApJ*, 534, 565
- Henry J. P., Evrard A. E., Hoekstra H., Babul A., Mahdavi A., 2009, *ApJ*, 691, 1307
- Heymans C., Van Waerbeke L., Bacon D., Berge J., Bernstein G., Bertin E., Bridle S., Brown M. L., Clowe D., Dahle H., Erben T., Gray M., Hetterscheidt M., Hoekstra H., Hudelot P., Jarvis M., Kuijken K., Margoniner V., Massey R., Mellier Y., Nakajima R., Refregier A., Rhodes J., Schrabback T., Wittman D., 2006, *MNRAS*, 368, 1323
- Hilbert S., Hartlap J., White S. D. M., Schneider P., 2009, *A&A*, 499, 31
- Hoekstra H., 2001, *A&A*, 370, 743
- , 2003, *MNRAS*, 339, 1155
- , 2007, *MNRAS*, 379, 317
- Hoekstra H., Jain B., 2008, *Annual Review of Nuclear and Particle Science*, 58, 99
- Hoekstra H., Mellier Y., van Waerbeke L., Semboloni E., Fu L., Hudson M. J., Parker L. C., Tereno I., Benabed K., 2006, *ApJ*, 647, 116
- Hoekstra H., Yee H. K. C., Gladders M. D., 2002, *ApJ*, 577, 595
- Ilbert O., Arnouts S., McCracken H. J., Bolzonella M., Bertin E., Le Fèvre O., Mellier Y., Zamorani G., Pellò R., Iovino A., Tresse L., Le Brun V., Bottini D., Garilli B., Maccagni D., Picat J. P., Scaramella R., Scodreggio M., Vettolani G., Zanichelli A., Adami C., Bardelli S., Cappi A., Charlot S., Ciliegi P., Contini T., Cucciati O., Foucaud S., Franzetti P., Gavignaud I., Guzzo L., Marano B., Marinoni C., Mazure A., Meneux B., Merighi R., Paltani S., Pollo A., Pozzetti L., Radovich M., Zucca E., Bondi M., Bongiorno A., Busarello G., de La Torre S., Gregorini L., Lamareille F., Mathez G., Merluzzi P., Ripepi V., Rizzo D., Vergani D., 2006, *A&A*, 457, 841
- Ilbert O., Capak P., Salvato M., Aussel H., McCracken H. J., Sanders D. B., Scoville N., Kartaltepe J., Arnouts S., Le Floc'h E., Mobasher B., Taniguchi Y., Lamareille F., Leauthaud A., Sasaki S., Thompson D., Zamojski M., Zamorani G., Bardelli S., Bolzonella M., Bongiorno A., Brusa M., Caputi K. I., Carollo C. M., Contini T., Cook R., Coppa G., Cucciati O., de la Torre S., de Ravel L., Franzetti P., Garilli B., Hasinger G., Iovino A., Kampanczyk P., Kneib J., Knobel C., Kovac K., Le Borgne J. F., Le Brun V., Fèvre O. L., Lilly S., Looper D., Maier C., Mainieri V., Mellier Y., Mignoli M., Murayama T., Pellò R., Peng Y., Pérez-Montero E., Renzini A., Ricciardelli E., Schiminovich D., Scodreggio M., Shioya Y., Silverman J., Surace J., Tanaka M., Tasca L., Tresse L., Vergani D., Zucca E., 2009, *ApJ*, 690, 1236
- Jain B., Seljak U., 1997, *ApJ*, 484, 560
- Jing Y. P., 2000, *ApJ*, 535, 30
- Komatsu E., Dunkley J., Nolte M. R., Bennett C. L., Gold B., Hinshaw G., Jarosik N., Larson D., Limon M., Page L., Spergel D. N., Halpern M., Hill R. S., Kogut A., Meyer S. S., Tucker G. S., Weiland J. L., Wollack E., Wright E. L., 2009, *ApJS*, 180, 330
- Mahdavi A., Hoekstra H., Babul A., Henry J. P., 2008, *MNRAS*, 384, 1567
- Mandelbaum R., Seljak U., Hirata C. M., 2008, *JCAP*, 8, 6
- Mantz A., Allen S. W., Rapetti D., Ebeling H., 2010, *MNRAS*, 1029
- Massey R., Heymans C., Bergé J., Bernstein G., Bridle S., Clowe D., Dahle H., Ellis R., Erben T., Hetterscheidt M., High F. W., Hirata C., Hoekstra H., Hudelot P., Jarvis M., Johnston D., Kuijken K., Margoniner V., Mandelbaum R., Mellier Y., Nakajima R., Paulin-Henriksson S., Peeples M., Roat C., Refregier A., Rhodes J., Schrabback T., Schirmer M., Seljak U., Semboloni E., van Waerbeke L., 2007, *MNRAS*, 376, 13
- Milkeraitis M., van Waerbeke L., Heymans C., Hildebrandt H., Dietrich J. P., Erben T., 2010, *MNRAS*, 406, 673
- Nagai D., Vikhlinin A., Kravtsov A. V., 2007, *ApJ*, 655, 98
- Navarro J. F., Frenk C. S., White S. D. M., 1995, *MNRAS*, 275, 720
- , 1997, *ApJ*, 490, 493
- Neto A. F., Gao L., Bett P., Cole S., Navarro J. F., Frenk C. S., White S. D. M., Springel V., Jenkins A., 2007, *MNRAS*, 381, 1450
- Okabe N., Takada M., Umetsu K., Futamase T., Smith G. P., 2010, *PASJ*, 62, 811
- Peacock J. A., Dodds S. J., 1996, *MNRAS*, 280, L19
- Rasia E., Ettori S., Moscardini L., Mazzotta P., Borgani S., Dolag K., Tormen G., Cheng L. M., Diaferio A., 2006, *MNRAS*, 369, 2013
- Schneider P., van Waerbeke L., Jain B., Kruse G., 1998, *MNRAS*, 296, 873
- Schrabback T., Hartlap J., Joachimi B., Kilbinger M., Simon P., Benabed K., Bradač M., Eifler T., Erben T., Fassnacht C. D., High F. W., Hilbert S., Hildebrandt H., Hoekstra H., Kuijken K., Marshall P. J., Mellier Y., Morganson E., Schneider P., Semboloni E., van Waerbeke L., Velander M., 2010, *A&A*, 516, A63+
- Seljak U., 2000, *MNRAS*, 318, 203
- Sheth R. K., Mo H. J., Tormen G., 2001, *MNRAS*, 323, 1
- Springel V., White S. D. M., Jenkins A., Frenk C. S., Yoshida N., Gao L., Navarro J., Thacker R., Croton D., Helly J., Peacock J. A., Cole S., Thomas P., Couchman H., Evrard A., Colberg J., Pearce F., 2005, *Nature*, 435, 629
- Van Waerbeke L., Mellier Y., Hoekstra H., 2005, *A&A*, 429, 75
- Vikhlinin A., Kravtsov A. V., Burenin R. A., Ebeling H., Forman W. R., Hornstrup A., Jones C., Murray S. S., Nagai D., Quintana H., Voevodkin A., 2009, *ApJ*, 692, 1060
- White M., van Waerbeke L., Mackey J., 2002, *ApJ*, 575, 640
- Wright C. O., Brainerd T. G., 2000, *ApJ*, 534, 34

